Improvement of Optical Quality and Vibration Characteristics of Injection Molded Disk with Processing Condition Control

Ji-Geun Nam, Hyo-Chol Sin, Sang-Sik Na

School of Mechanical and Aerospace Engineering, Seoul National University, San 56–1, Sinlim-dong, Kwanak-gu, Seoul, 151–744, Korea

Received 4 October 2004; accepted 18 October 2005
DOI 10.1002/app.23750
Published online in Wiley InterScience (www.interscience.wiley.com).

ABSTRACT: Increased application of optical disks has required a rotating disk with more dynamic stability and better optical quality. A new concept of controlling the processing condition of injection molded disks is developed to improve their optical quality and vibration characteristics. To assess the effect of process conditions on residual stresses, birefringence, and critical speed, an orthogonal array for design of experiments is used. Melt temperature, filling speed, and packing pressure were effective parameters, but mold temperature and interactions among process conditions were not. The birefringence and critical speed were affected by the residual stress distribution, which varied according to the distance from the gate and processing condition. Considering the effect of the processing conditions and distance from the gate, we calculated the weight factors on residual stresses along the radial direction. Choosing weighted stress to be the target value for optimization of residual stresses, processing conditions control was accomplished. Under the newly proposed conditions, optical quality and stability of injection molded disk were simultaneously improved. © 2006 Wiley Periodicals, Inc. J Appl Polym Sci 101: 3275–3285, 2006

Key words: birefringence; critical speed; injection molding; optimization

INTRODUCTION

With increasing application of optical disks for data storage devices, the data access speed and the data storage density of optical devices also need to be increased. To safely access high density data at high speed, we need a rotating disk with dynamic stability and improved optical quality. The optical quality and dynamic stability of the molded disk are affected by flow-induced residual stresses, which orient the molecular chain in the disk during cavity filling. Therefore, a new concept for injection molding process to control residual stresses must be developed to produce better optical quality and dynamic stability of disks.

Many studies have tried to predict flow-induced birefringence, which is related to flow stresses, in injection molded parts. In analyzing flow-induced residual stresses and birefringence, many researchers have employed the Leonov constitutive model[1,2] to describe the nonlinear viscoelastic nature of polymer melt. This model was used to develop theoretical approaches that could predict the residual stresses and birefringence in various geometries[3–6] and to study the effect of processing condition for birefringence.[7–10] Also, some experimental research has been reported for birefringence distribution in a center-gated disk and magneto-optical disk.[11,12]

The vibration of rotating circular disks must be accurately characterized, especially in terms of the critical speed and the characteristics of the frequency. Since the study of Lamb and Southwell,[13] vibration and stability of a spinning circular disk have been continually investigated. Mote and coworkers[14,15] studied a method to increase rotating speed and critical speed by applying initial stresses to a circular saw. The critical speed of disks has been increased by methods such as changing the initial stresses by using a thin circular ring called roll tensing,[16] applying various initial stresses patterns,[17] and changing the inner boundary condition of a disk according to the rotating speed.[18] The vibration characteristics of flexible disks subjected to a transverse load have been studied.[19–21] Recently, there has been work on increasing stiffness and critical speed of disk by controlling residual stresses and by changing injection molding processing condition.[22]

We applied a numerical simulation system developed for the injection molding process to a center-gated disk, by considering filling, packing, cooling process, and predicted flow-induced residual stresses and birefringence by using the Leonov model and stress optical law.[23] By adopting residual stresses as initial stresses, natural frequency and critical speed of disk were analyzed. Using an orthogonal array for design of experiments,[24] the effect of processing con-

Correspondence to: H. C. Sin (sinhyo@snu.ac.kr).

ditions on birefringence, residual stresses, and critical speed was assessed. Through this approach, we propose a processing conditions for improving both the optical quality and vibration characteristics of rotating disks.

THEORETICAL FORMULATIONS

Injection molding analysis

Governing equations

The mathematical modeling and the assumptions used to analyze the injection molding processes are similar to those of previous studies.[3–10]

1. The velocity component v_z in the gapwise direction is neglected.
2. Thermal conductivity k is a constant.
3. Convection heat transfer in the thickness direction and conduction heat transfer in the planar direction are neglected. Only heat transfer by conduction in the thickness direction is considered.
4. Heat transfer by fountain flow in melt front is neglected.
5. The core and mold are assumed to be symmetric through gap thickness.

With these assumptions, the governing equations can be written as follows[25]:

Continuity equation:

$$\frac{\partial \rho}{\partial t} + \frac{\partial}{\partial x}(\rho v_x) + \frac{\partial}{\partial y}(\rho v_y) = 0 \tag{1}$$

Momentum equations:

$$0 = -\frac{\partial p}{\partial x} + \frac{\partial \tau_{xz}}{\partial z} \tag{2a}$$

$$0 = -\frac{\partial p}{\partial y} + \frac{\partial \tau_{yz}}{\partial z} \tag{2b}$$

$$0 = -\frac{\partial p}{\partial z} + \frac{\partial \tau_{zz}}{\partial z} \tag{2c}$$

Energy equation:

$$\rho C_p\left(\frac{\partial}{\partial t} + v_x\frac{\partial T}{\partial x} + v_y\frac{\partial T}{\partial y}\right) = \frac{\partial}{\partial z}\left(k\frac{\partial T}{\partial z}\right) + \Phi \tag{3}$$

where x and y are the planar directions and z is the gapwise direction, and νx, νy are velocity components in each direction. C_p, k, Φ, and ρ are specific heat, thermal conductivity, dissipation-function, and density, respectively. Density is given as follows[26,27]:

$$\rho(P,T) = \rho_0(T)\left\{1 - C\ln\left[1 + \frac{T}{B(T)}\right]\right\}^{-1} \tag{4}$$

The parameters in eq. (4) are defined as follows:

$$C = 0.0894 \tag{5}$$

$$\frac{1}{\rho_0(T)} = \begin{cases} b_{1,l} + b_{2,l}(T - b_5) & \text{if } T > T_t \\ b_{1,x} + b_{2,s}(T - b_5) & \text{if } T < T_t \end{cases} \tag{6}$$

$$B(T) = \begin{cases} b_{3,l}\, exp(-b_{4,l}(T - b_5)) & if\ T > T_t \\ b_{3,x}\, exp(-b_{4,s}(T - b_5)) & if\ T < T_t \end{cases} \tag{7}$$

$$T_t = b_5 + b_6 p \tag{8}$$

Dissipation-function is as follows[28]:

$$\Phi = 2\eta_0 s \cdot \mathrm{tr}\, \underline{\underline{e}}^2 + \sum_k \frac{\eta_k}{4\theta_k^2}\left[\frac{I_1(I_2 - I_1)}{3} + \mathrm{tr}\underline{\underline{C}}_k^2 - 3\right] \tag{9}$$

where $\underline{\underline{e}} = \frac{1}{2}(\nabla \mathbf{v} + \nabla \mathbf{v}^T)$

$\mathbf{v}$ is the velocity vector, I_1 and I_2 are the invariants of the elastic strain tensor c_k, and θ_k, η_k, and s are defined in the following section.

The boundary conditions associated with the governing equations are as follows:

$$v_x = v_y = 0 \quad \text{at } z = \pm h \tag{10a}$$

$$T = T_W \quad \text{at } z = \pm h \tag{10b}$$

$$\frac{\partial v_x}{\partial z} = \frac{\partial v_y}{\partial z} = 0 \quad \text{at } z = 0 \tag{10c}$$

$$\frac{\partial T}{\partial z} = 0 \quad \text{at } z = 0 \tag{10d}$$

$$P = 0 \quad \text{at the melt front} \tag{10e}$$

where h is the half-gap thickness.

Constitutive equations

The Leonov model was employed as a constitutive equation.[1,2]

$$\underline{\underline{\tau}} = -P\underline{\underline{\delta}} + s\eta_0(\nabla \mathbf{v} + \nabla \mathbf{v}^T) + \sum_{k=1}^{N}\frac{\eta_k}{\theta_k}\underline{\underline{C}}_k \tag{11}$$

$$\eta_0 = \sum_{k=1}^{N}\frac{\eta_k}{1 - s} \tag{12}$$

where s is a rheological parameter lying between zero and one, and η_k, θ_k, C_k, are kth mode shear viscosity, relaxation time, and elastic strain tensor, respectively, and η_0 is the zero-shear-rate viscosity. To consider the dependence of η_k and θ_k, on the temperature change, the WLF-shift factor is employed. Then,

$$\theta_k = \theta_k(T_0)\frac{a_T}{a_{T_0}} \tag{13}$$

$$\eta_k = \eta_k(T_0)\frac{a_T}{a_{T_0}} \tag{14}$$

$$a_T\begin{cases} a_{T_0} & T \le T_g \\ \exp\left[-\dfrac{c_1(T-T_{\text{ref}})}{c_2+T-T_{\text{ref}}}\right] & T > T_g \end{cases} \tag{15}$$

where T_{ref} and T_g are the reference temperature and glass transition temperature, respectively, and c_1, c_2 are constants.

In addition, the evolution equation of the elastic strain tensor $\underline{\underline{C}}_k$ is as follows:

$$\frac{D\underline{\underline{C}}_k}{Dt} - \nabla\mathbf{v}^T\cdot\underline{\underline{C}}_k - \underline{\underline{C}}_k\cdot\nabla_{\mathbf{v}} + \frac{1}{2\theta_k}(\underline{\underline{C}}_k\cdot\underline{\underline{C}}_k - \underline{\underline{\delta}}) = 0 \tag{16}$$

where $\frac{D\underline{\underline{C}}_k}{Dt}$ is the substantial derivative of $\underline{\underline{c}}_k$ with respect to time.

$$\frac{D\underline{\underline{C}}_k}{Dt} = \frac{\partial}{\partial t}\underline{\underline{C}}_k + \mathbf{v}\cdot\nabla\underline{\underline{C}}_k \tag{17}$$

Numerical formulation

For simulation of the injection molding process, the following numerical formulation is applied[26–28]:

By substituting eq. (11) into eqs. (2a) and (2b), and integrating the results with respect to the thickness, and applying boundary conditions, the velocity gradients are as follows:

$$\frac{\partial v_x}{\partial z} = \frac{\partial P}{\partial x}\frac{z}{\eta_x} \tag{18}$$

$$\frac{\partial v_y}{\partial z} = \frac{\partial P}{\partial y}\frac{z}{\eta_y} \tag{19}$$

where

$$\eta_x = \eta_0 s + \frac{1}{\dfrac{\partial v_x}{\partial z}}\sum_{k=1}^{N}\frac{\eta_k}{\theta_k}C_{xz,k} \tag{20}$$

$$\eta_y = \eta_0 s + \frac{1}{\dfrac{\partial v_y}{\partial z}}\sum_{k=1}^{N}\frac{\eta_k}{\theta_k}C_{yz,k} \tag{21}$$

Substitution of eqs. (20) and (21) into eqs. (18) and (19) results in the velocity gradient as:

$$\frac{\partial v_x}{\partial z} = \frac{1}{\eta_0 s}\left(\frac{\partial P}{\partial x}z - \sum_{k=1}^{N}\frac{\eta_k}{\theta_k}C_{xz,k}\right) \tag{22}$$

$$\frac{\partial v_x}{\partial z} = \frac{1}{\eta_0 s}\left(\frac{\partial P}{\partial y}z - \sum_{k=1}^{N}\frac{\eta_k}{\theta_k}C_{yz,k}\right) \tag{23}$$

Integrating eqs. (18) and (19) and using the boundary conditions,

$$v_x = -\frac{\partial P}{\partial x}\int_z^h \frac{z}{\eta_x}dz \tag{24}$$

$$v_y = -\frac{\partial P}{\partial y}\int_z^h \frac{z}{\eta_y}dz \tag{25}$$

With the substitution of eqs. (24) and (25) into eq. (1), the governing equation becomes

$$G\frac{\partial P}{\partial r} + H - \frac{\partial}{\partial x}\left(S_x\frac{\partial P}{\partial x}\right) - \frac{\partial}{\partial y}\left(S_y\frac{\partial P}{\partial y}\right) = 0 \tag{26}$$

where

$$G = \int_0^h\left(\frac{\partial\rho}{\partial P}\right)dz \tag{27}$$

$$H = \int_0^h\left(\frac{\partial\rho}{\partial T}\right)\left(\frac{\partial T}{\partial t}\right)dz \tag{28}$$

$$S_x = \int_0^h\left(z\int_0^z\rho dz'\right)\frac{dz}{d\eta_x} \tag{29}$$

$$S_y = \int_0^h\left(z\int_0^z\rho dz'\right)\frac{dz}{d\eta_y} \tag{30}$$

The initial values of C_k that represent the first entrance of polymer melt into the mold cavity are determined from the fully developed steady-state solution $\frac{dC_k}{dt} = 0$, under isothermal conditions.

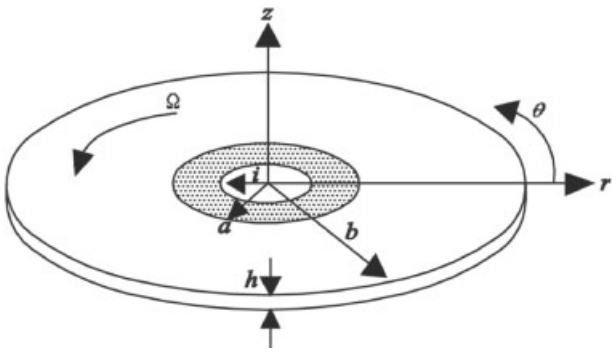

Figure 1 Schematic of a rotating disk.

The finite element method, with triangular elements and linear shape function, is used to solve eq. (26). The governing equations are calculated in Cartesian coordinates. For circular disks, constitutive equations are solved in the cylindrical streamwise coordinate system (r, θ, z), using methods proposed by Shyu et al.[28]

For isotropic materials, the difference in the refractive index along the optical principal axis is proportional to that of the principal stresses, a relation called the stress-optical law.[23] The flow-induced birefringence can be calculated in the rz plane according to the stress-optical law as follows:

$$\Delta n = C_\sigma^{\mathrm{fl}} \sqrt{(\sigma_{rr} - \sigma_{zz})^2 + 4\tau_{rz}^2} \tag{31}$$

where C_σ^{fl} is the stress-optical coefficient at the melt state.

Modal analysis of rotating disk

Governing equation

The disk, as shown in Figure 1, is fixed from inner radius (i) to the clamping radius (a) and free at the outer radius (b); thickness and rotating speed are h and Ω, respectively; the material of disk is isotropic and elastic.

Denoting the lateral displacement of the plate by w, the equation of motion with respect to the coordinate frame (r, θ) is as follows:[19]

$$\rho h\left(\frac{\partial^2 w}{\partial t^2} + 2\Omega\frac{\partial^2 w}{r\partial t\partial\theta} + \Omega\frac{\partial^2 w}{\partial\theta^2}\right) + \nabla^2(D\nabla^2 w) - \frac{\partial}{r\partial r}\left(r\sigma_r\frac{\partial w}{\partial r}\right) - \frac{\partial}{r\partial\theta}\left(\sigma_\theta\frac{\partial w}{r\partial\theta}\right) = 0 \tag{32}$$

where $D = Eh^3/12(1 - \nu^2)$; E is the Young's modulus, ν the Poisson's ratio.

In eq. (32), σ_r and σ_θ are stresses in the radial and hoop direction, respectively, and can be divided into initial (residual) stresses and rotational stresses as follows[19]:

$$\sigma_i = \sigma_i^{\mathrm{rotational}} + \sigma_i^{\mathrm{residual}}, \quad i = r,\theta \tag{33}$$

$$\sigma_r^{\mathrm{rotational}} = \frac{\rho\Omega^2 b^2}{8}\left(A_1 + \frac{A_2}{(r/b)^2} - (3+\nu)\left(\frac{r}{b}\right)^2\right) \tag{34}$$

$$\sigma_0^{\mathrm{rotational}} = \frac{\rho\Omega^2 b^2}{8}\left(A_1 - \frac{A_2}{(r/b)^2} - (1+3\nu)\left(\frac{r}{b}\right)^2\right) \tag{35}$$

where A_1, A_2 are

$$A_1 = (1+\nu)\frac{(3+\nu) + (1-\nu)(a/b)^4}{(1+\nu) + (1-\nu)(a/b)^2} \tag{36}$$

$$A_2 = (1-\nu)\left(\frac{a}{b}\right)^2\frac{(3+\nu) - (1-\nu)(a/b)^2}{(1+\nu) + (1-\nu)(a/b)^4} \tag{37}$$

The disk is fully clamped at the radius $r = a$, while free along the outer edge $r = b$; therefore, the displacement conditions hold at a and the force and moment conditions hold at b. The boundary conditions are as follows[29,30]:

$$w = \frac{\partial w}{\partial r} = 0 \quad (r = a) \tag{38}$$

$$\frac{\partial}{\partial r}\nabla^2 w + (1-\nu)\frac{\partial^2}{r^2\partial\theta^2}\left(\frac{\partial w}{\partial r} - \frac{w}{r}\right) = 0 \tag{39}$$

$$\frac{\partial_2 w}{\partial r_2} + \nu\left(\frac{\partial w}{r\partial r} + \frac{\partial^2 w}{r^2\partial\theta^2}\right) = 0 \quad (r = b)$$

For calculation of natural frequency, Rayleigh–Ritz approximation method[31] was used. Assuming the transverse displacement as follows:

$$w_n(r,\theta,t) = \phi_n(r)\cos n\theta\cos\omega_n t \tag{40}$$

and substituting eq. (40) into eq. (32), one can obtain the following equation.[29]

$$\delta\left\{\int_0^{2\pi}\int_a^b \rho\left(\frac{\partial w_n}{\partial t}\right)^2 + 2\rho\Omega\frac{\partial w_n}{\partial t}\frac{\partial w_n}{\partial\theta} + \rho\left(\Omega\frac{\partial w_n}{\partial\theta}\right)^2 - \sigma_r\left(\frac{\partial w_n}{\partial r}\right)^2 - \sigma_\theta\left(\frac{\partial w_n}{r\partial\theta}\right)^2 - \frac{D}{2h}\left[(\nabla^2 w_n)^2 - 2(1-\nu)\left(\frac{\partial^2 w_n}{\partial r^2}\left[\frac{1}{r}\frac{\partial w_n}{\partial r} + \frac{1}{r^2}\frac{\partial^2 w_n}{\partial\theta^2}\right] - \left[\frac{\partial}{\partial r}\left(\frac{1}{r}\frac{\partial w_n}{\partial\theta}\right)\right]^2\right)\right] hrdrd\theta\right\} = 0 \tag{41}$$

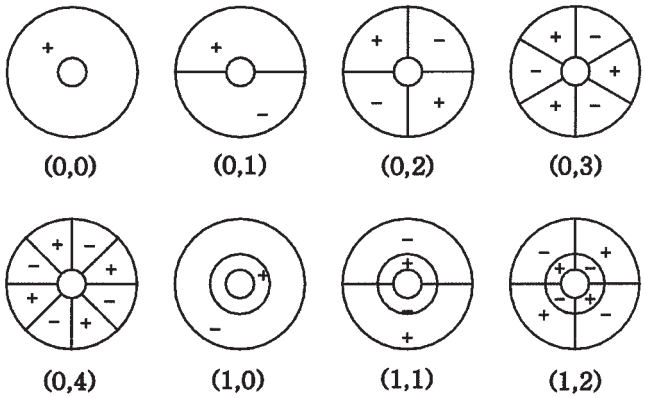

Figure 2 Mode shapes of a rotating disk.

After substituting eqs. (33) and (40) into eq. (41), by numerical integration one can calculate ω_n.

In eq. (40), $\phi_n(r)$ is assumed to be the following function:

$$\phi_u(r) = (r - a)^2(1 + c_1 r + c_2 r^2) \tag{42}$$

where c_1, c_2 are to be determined by the natural boundary conditions [eq. (39)]. Then, w_n given in eq. (40) automatically satisfies the geometric boundary of eq. (38).

Critical speed of rotating disk

The mode shapes of the vibration of a circular disk are axisymmetric and asymmetric and the modes have nodal lines, at which the transverse displacement of the disk is zero. Nodal lines take the shape of a circle in the axisymmetric mode and of a line in asymmetric one, which are called nodal circle (nc) and nodal diameter (nd), respectively. In this study, modal index (m, n) was used, where m and n is the number of nodal circles and nodal diameters, respectively. Mode index and mode shape are shown in Figure 2.

By solving eq. (41), the natural frequency of the n nodal diameter mode can be expressed as follows:[19,30]

$$\omega_n^2 = \omega_{\text{sn}}^2 + \Omega^2(\alpha_n + n^2\beta_n) \tag{43}$$

where ω_{sn} is the natural frequency when the disk is stationary, and α_n, β_n are nondimensional parameters related to the in-plane stress caused by rotation. The natural frequency, as shown in Figure 3, is divided into the forward traveling wave and the backward traveling wave, and can be expressed as follows:[30]

$$\omega_n^f = |\sqrt{\omega_{\text{sn}}^2 + \Omega^2(\alpha_n^2 + n^2\beta_n^2)} + n\Omega| \tag{44}$$

$$\omega_n^b = |\sqrt{\omega_{\text{sn}}^2 + \Omega^2(\alpha_n^2 + n^2\beta_n^2)} - n\Omega| \tag{45}$$

As the rotation speed of the disk increases, the natural frequencies for the backward traveling wave decrease and finally reach zero. Physically, this behavior means that resonance appears in the system when the disk is subjected to a stationary (zero frequency) lateral load. The speed of rotation that brings about this type of instability is generally referred to as the critical speed.

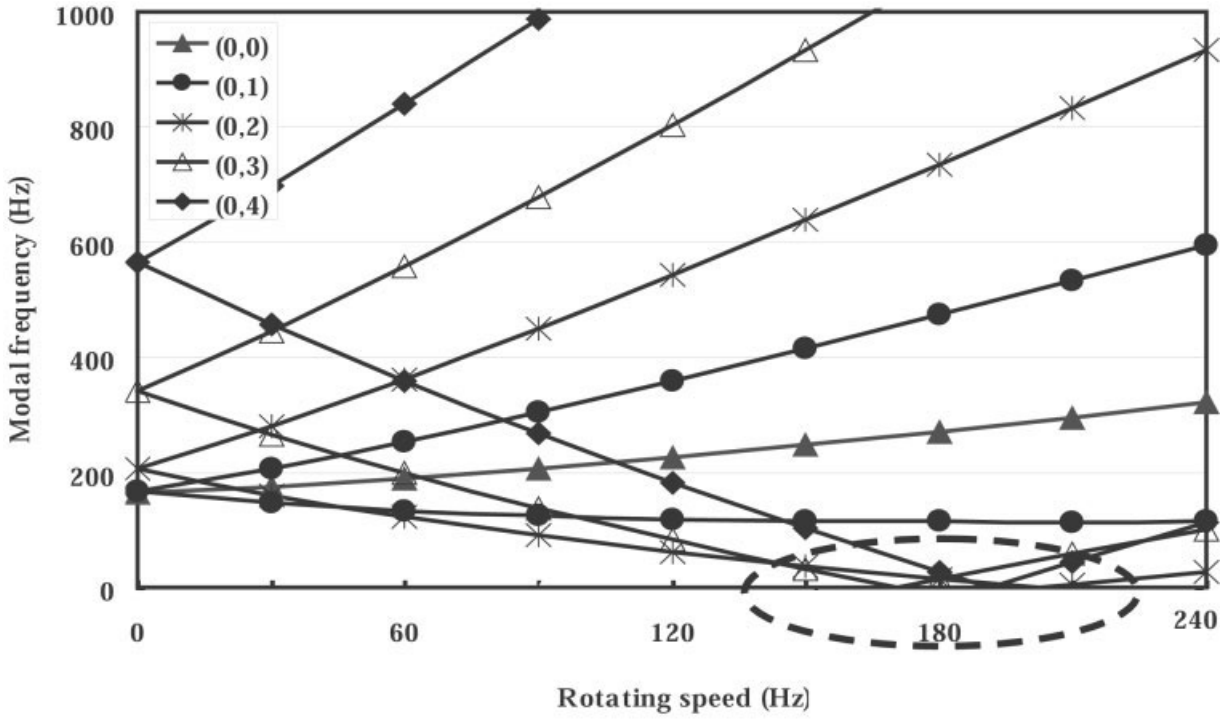

Figure 3 Modal frequencies of a rotating disk.

TABLE I
Critical Speed of Some Rotating Modes with Initial Stresses

Mode	Speed (Hz)
(0,0)	∞
(0,1)	∞
(0,2)	201
(0,3)	170
(0,4)	191

When a circular disk rotates in high speed above the critical speed, fluttering appears. In fluttering, the flow of circumferential air excites the mode of the backward traveling wave, and then the amplitude of vibration increases greatly, and fatal errors occur in reading and writing data. Therefore, dynamic stability must be maintained by increasing the critical speed and stiffness. Table I shows the critical speed of each mode. Assuming the disk, shown in Figure 1, has a radial residual stress of a 0.5 MPa, the critical speed of disk is calculated. The dimensions of disk are given in the following section. Note that (0,0) and (0,1) modes do not have a critical speed. For a rotating disk with initial stresses, because the vibration mode which brings the lowest critical speed is transferred from (0,3) mode to other modes, the critical speed of (0,3) mode was considered in this study.

INVESTIGATION OF EFFECTIVE PROCESSING CONDITION BY THE DESIGN OF EXPERIMENTS

To predict the flow-induced residual stresses and birefringence, the filling, packing, and cooling processes were considered. When the temperature of a material is below $T_{frz}(= T_R + 30)$, it is assumed that a portion of it ceases to flow. Also, when the temperature of an entire material in the mold reaches the glass transition temperature, the product is ejected. Once the flow-induced residual stresses and birefringence are determined from injection molding simulation, then the residual stresses can be considered as initial stresses in the disk. Because the variations of stress along the direction of gap thickness hardly affect disk vibration, the disk was modeled as a shell type. For rotating disks from 0 Hz to 240 Hz, the modal frequency and critical speed were calculated.

To investigate the effect of processing conditions on birefringence, residual stresses, and critical speed of the injection molded disk, an orthogonal array ($L_{27}(3^{13})$) was chosen for the design of experiments for simulation.[31] Four factors were considered: melt temperature (A), mold temperature (B), filling speed (C), and packing

TABLE II
The Layout of Orthogonal Array $L_{27}(3^{18})$ for the Design of Experiments

	Control factor												
No.	A	B	A B	A B	D	A D	A D	B D	C	e	B D	e	e
1	0	0	0	0	0	0	0	0	0	0	0	0	0
2	0	0	0	0	1	1	1	1	1	1	1	1	1
3	0	0	0	0	2	2	2	2	2	2	2	2	2
4	0	1	1	1	0	0	0	1	1	1	2	2	2
5	0	1	1	1	1	1	1	2	2	2	0	0	0
6	0	1	1	1	2	2	2	0	0	0	1	1	1
7	0	2	2	2	0	0	0	2	2	2	1	1	1
8	0	2	2	2	1	1	1	0	0	0	2	2	2
9	0	2	2	2	2	2	2	1	1	1	0	0	0
10	1	0	1	2	0	1	2	0	1	2	0	1	2
11	1	0	1	2	1	2	0	1	2	0	1	2	0
12	1	0	1	2	2	0	1	2	0	1	2	0	1
13	1	1	2	0	0	1	2	1	2	0	2	0	1
14	1	1	2	0	1	2	0	2	0	1	0	1	2
15	1	1	2	0	2	0	1	0	1	2	1	2	0
16	1	2	0	1	0	1	2	2	0	1	1	2	0
17	1	2	0	1	1	2	0	0	1	2	2	0	1
18	1	2	0	1	2	0	1	1	2	0	0	1	2
19	2	0	2	1	0	2	1	0	2	1	0	2	1
20	2	0	2	1	1	0	2	1	0	2	1	0	2
21	2	0	2	1	2	1	0	2	1	0	2	1	0
22	2	1	0	2	0	2	1	1	0	2	2	1	0
23	2	1	0	2	1	0	2	2	1	0	0	2	1
24	2	1	0	2	2	1	0	0	2	1	1	0	2
25	2	2	1	0	0	2	1	2	1	0	1	0	2
26	2	2	1	0	1	0	2	0	2	1	2	1	0
27	2	2	1	0	2	1	1	1	0	2	0	2	1

TABLE III
Properties of Polystyrene Styron 615APR DOW and Mold[2,7,9]

PVT model coefficient	$b_{1l} = 0.947\ cm^3/g$	$b_{1s} = 0.947\ cm^3/g$
	$b_{2l} = 5.920 \times 10^{-4}\ cm^3/g\ K$	$b_{2s} = 2.470 \times 10^{-4}\ cm^3/g\ K$
	$b_{3l} = 1.699$ Pa	$b_{3s} = 2.489$ Pa
	$b_{4l} = 4.132 \times 10^{-3}\ K^{-1}$	$b_{4s} = 4.257 \times 10^{-3}\ K^{-1}$
	$b_s = 367.15$ K	
	$b_b = 2.740$ K/Pa	
	$T_0 = 463$ K, $N = 2$, $s = 0.09$	
Rheological parameters	$\theta_1 = 0.80$ s, $\eta_1 = 5.44 \times 10^4$ *g/cm s*	
	$\theta_2 = 0.027$ s, $\eta_2 = 1.5 \times 10^4$ *g/cm s*	
WLF-shift factor	$c_1 = 25.391$ K, $c_2 = 51.6$ K	
	$T_{ref} = 373.15$ K	
Glass transition temperature	$T_g = 373$ K	
Thermal conductivity	$k = 0.15$ W/(mK)	
Specific heat capacity	$C_p = 2100$ J/(kg K)	
Stress-optical coefficient	$C = 4.8 \times 10^{-9}\ Pa^{-1}$	
Young's Modulus	$E = 2.283$ GPa	
Poisson's ratio	$v = 0.36$	
Mold properties	Density	$\rho = 7.85\ g/cm^3$
	Specific heat	$C_{pm} = 462$ J/(kg K)
	Thermal conductivity	$k_m = 24.3$ W/(mK)

pressure (D). Each factor has three levels. During the layout of an orthogonal array, three pairs of interactions among factors were considered in addition to the four main factors. The first pair was the interaction between the melt temperature and mold temperature, which was assigned to columns 3 and 4. The second pair was the interaction between the melt temperature and packing pressure, which was assigned to columns 6 and 7. The last pair was the interaction between the mold temperature and packing pressure, which was assigned to columns 8 and 11. The completed simulation design is shown in Table II.

Birefringence, residual stresses, and critical speed at three positions were assigned to be the response factor. Because the increase in the critical speed by shear stresses was less than that by the radial and hoop stresses, the radial and hoop component of the residual stress were selected to be a response factor.

A center-gated disk shown in Figure 1 was chosen for the analysis of injection molding and vibration: inner, outer, and clamping radii were 0.75, 6, 1.5, respectively; and thickness was 1.2 mm. To compare our data with the existing experimental[11] and numerical[3,7,28] results, polystyrene (Styron 615APR/Dow) was used in all of the simulations. The material properties of polystyrene, mold properties, and processing conditions are shown in Tables III and IV, respectively. Injection molding machine used in analysis was Summitomo Disc 3, which is mainly used in producing a circle shape. In Table IV, packing pressures are given in proportion to maximum pressure at the end of filling as 0, 50, 90%. Packing pressures in Tables V and VI have the same meaning. For the finite element analysis, 1096 triangular elements and 589 nodes were used.

RESULTS AND DISCUSSION

The effective factor for birefringence, residual stresses, and critical speed of the disk

We have numerically analyzed the effect of processing conditions on birefringence, residual stresses, and critical speed of the injection molded disk. The interactions among any pair of the factors were not significant and the response factors vary along the radial location. After pooling nonsignificant factors with the error, the mean values of birefringence and residual stresses were estimated; the variations of those values are illustrated in Figures 4–8.

The effect of each factor is as follows:

Melt temperature (a). In the filling stage, hot melt enters the mold cavity. Once the melt contacts the cold cavity wall, the layer near the cavity wall starts to cool down. Within the solidified layer, where melt temper-

TABLE IV
Three Levels of Effective Factors for Experimental Variance

	1	2	3
Melt temperature (°C)	208	218	228
Mold temperature (°C)	25	35	45
Flow rate (cm^3/s)	11.9	23.8	35.7
Packing pressure (%)	0	50	90

TABLE V
Initial and Optimal Process Conditions

	T_{melt} (°C)	T_{mold} (°C)	Q_{inf} (cm^3/s)	P_{pack} (%)
Initial condition	240	35	13.6	90
Optimal condition	234	35	31.2	45

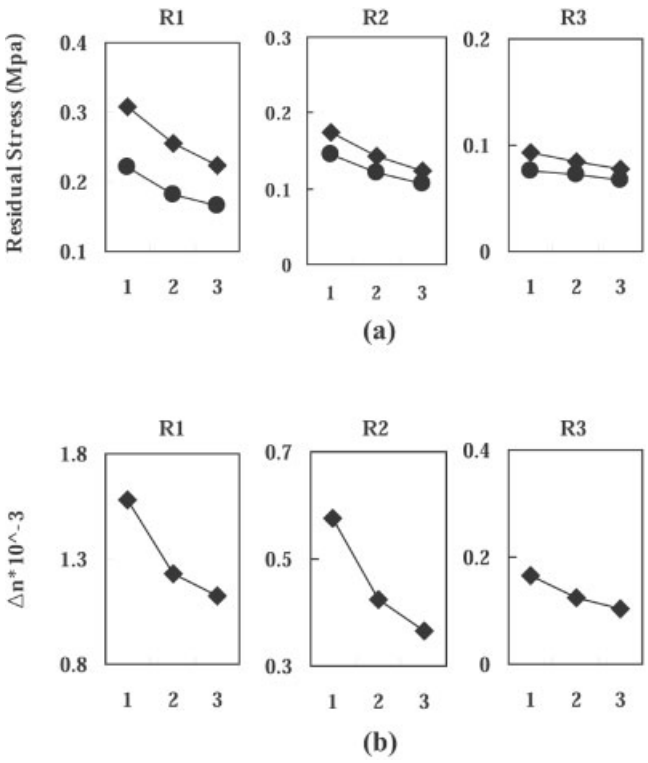

Figure 4 The response diagram for the three levels of melt temperature; (a) residual stress: (♦)σ_{rr}, (●)$\sigma_{\theta\theta}$; (b) gapwise average birefringence; R1 = 18.5 mm, R2 = 36.5 mm, R3 = 55.4 mm.

ature is below the glass transition temperature, flow-induced stresses become frozen-in and almost do not relax and remain to the end of the latter injection molding stage. But stresses relax in the layer near the cavity core where the melt is still hot in the beginning of the cooling phase. When melt temperature increases, the solidified thickness decreases and stresses relax at more locations. More relaxation occurs during packing and cooling process, and the melt becomes more fluid, and its viscosity and shear stresses decrease. Therefore, as shown in Figure 4, residual stresses and birefringence are lower at all locations when the melt temperatures increase.

Mold temperature (b). Like the melt temperature, when the mold temperature increases the solidified thickness decreases, and the associated residual stresses and birefringence decrease. However, the effect of this parameter is very small compared with the melt temperature as seen in Figure 5.

Filling speed (c). Figure 6(a) shows that the effect of filling speed on residual stresses is different according to radial position. At the high injection speed, the velocity profile becomes more sharply distributed with the increase of peak value at the gap center, and the associated residual stresses are also increased accordingly. When the injection speed is high; however, the contact time with mold wall reduces, resulting in higher melt temperature at the end of the filling process. Thus, the thickness of solidified layers decreases; residual stresses are reduced.

Near the gate area, the contact time is longer and the thickness of solidified layer is larger than that away from the gate; the contact time affects the residual stresses more significantly than the velocity profile does. Therefore, when the filling speed is higher, the residual stresses decrease at the gate area. Meanwhile, at the area away from gate, because the effect of the velocity profile is a more important factor, the residual stresses at this area increase when the filling speed increases.

The birefringence, which is represented by the difference of principal stresses, decreases throughout the entire region when the filling speed increases as seen in Figure 6(b). So, it can be thought that the difference of principal stresses is mainly affected by the contact time.

Packing pressure (d). At the packing stage, the residual stresses and the birefringence in the solidified layer are not changed by packing pressure. While the melt is still hot in the core layers, the additional material flows into the cavity, and subsequently, stress relaxes. As shown in Figure 7, higher packing pressure leads to more additional flow, which increases birefringence and residual stresses. Because the magnitude of the additional flow is proportional to the pressure in the melt, the closer to the gate, the greater is the effect of packing pressure.

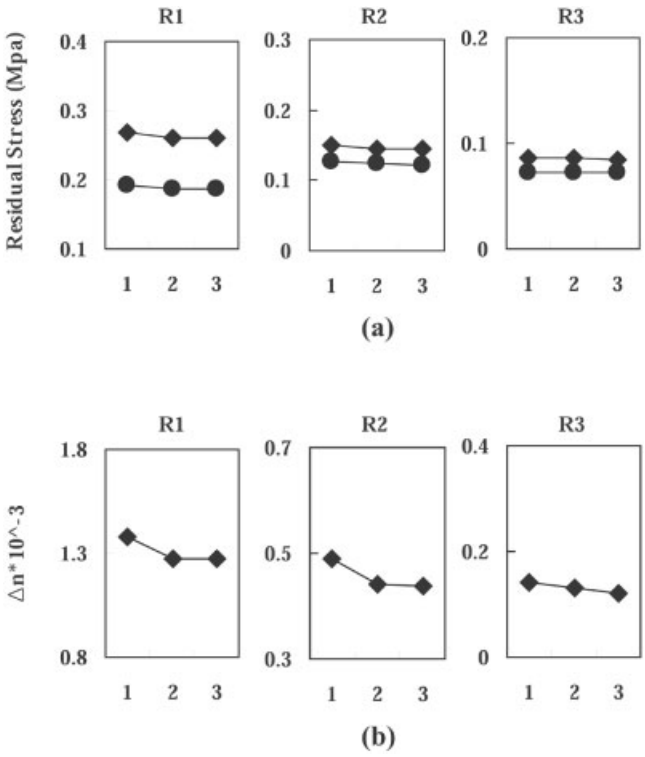

Figure 5 The response diagram for the three levels of mold temperature; (a) residual stress: (♦)σ_{rr}, (●)$\sigma_{\theta\theta}$; (b) gapwise average birefringence; R1 = 18.5 mm, R2 = 36.5 mm, R3 = 55.4 mm.

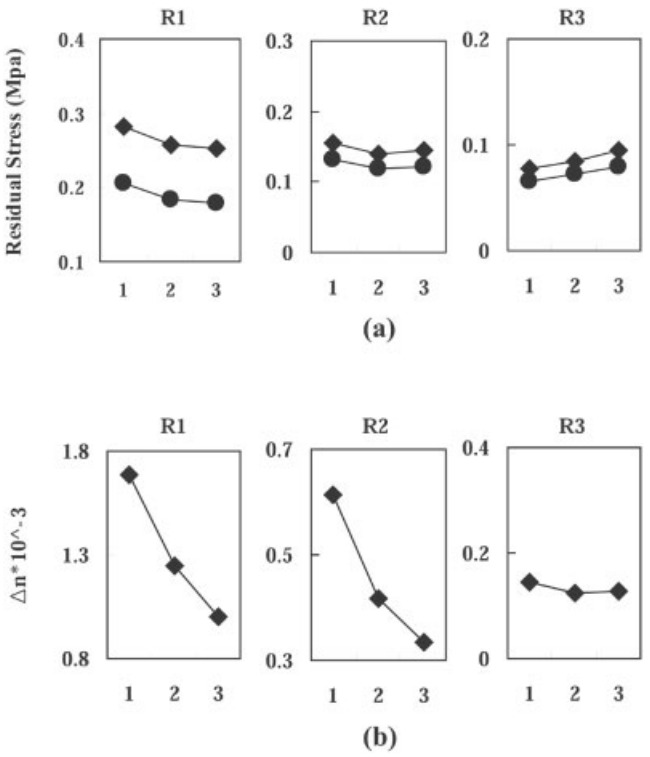

Figure 6 The response diagram for three levels of filling speed; (a) residual stress: (♦)σ_{rr}, (●)$\sigma_{\theta\theta}$; (b) gapwise average birefringence; R1 = 18.5 mm, R2 = 36.5 mm, R3 = 55.4 mm.

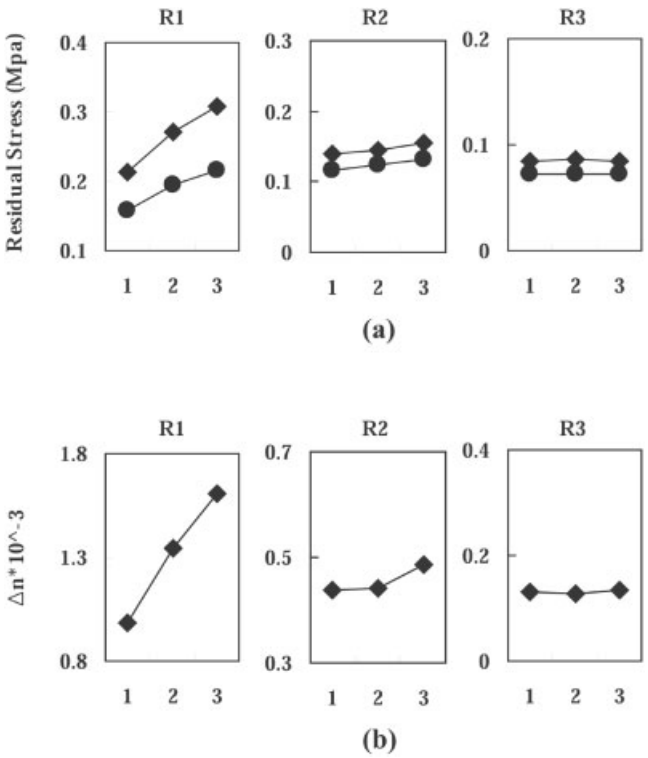

Figure 7 The response diagram for the three levels of packing pressure; (a) residual stress: (♦)σ_{rr}, (●)$\sigma_{\theta\theta}$; (b) gapwise average birefringence; R1 = 18.5 mm, R2 = 36.5 mm, R3 = 55.4 mm.

Effect on critical speed. Generally, the critical speed increases when residual stresses are added to the rotating disk. Therefore, as shown in Figure 8, critical speed varies similarly to that of residual stress; higher melt temperature drops the critical speed; mold temperatures hardly affect the critical speed; also, as packing pressure and filling speed increase, the critical speed increased.

Improvement of optical quality and stability by means of controlling the process condition

Birefringence and critical speed are affected by residual stresses, which vary as functions of radial position and processing condition. By controlling residual stresses, optical and vibration characteristics can be improved. This idea was applied to the compact disk, which was analyzed in the previous section.

To examine the effect of residual stress on the critical speed as a function of distance from the gate, the increase in the critical speed by residual stress at each radial position was calculated. Generally, residual stresses and birefringence are larger near the gate area than those at other positions, because the velocity of the melt front and the thickness of the solidified layers are larger in the filling stage. Nevertheless, the increase of critical speed at the outer radius position by residual stresses increases more than that at the inner radius near the clamped position. Hence, by reducing the residual stress at the gate area and increasing it at the outer radius positions, the average residual stress and birefringence in injection molded disk can be decreased, and the critical speed, which is representing the stiffness of the disk, can be increased. With the following equation, an increase of critical speed by residual stresses at each position is converted to weight factors, which are shown in Figure 9.

$$WF_i = \frac{\Delta CS_i}{\text{ave}(\Delta CS_i)} \tag{46}$$

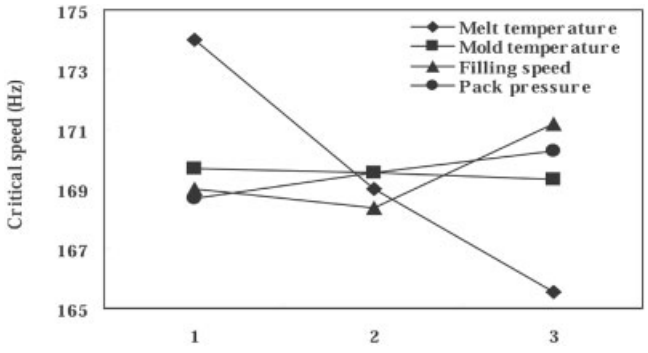

Figure 8 The variation of critical speed for the three levels of processing condition.

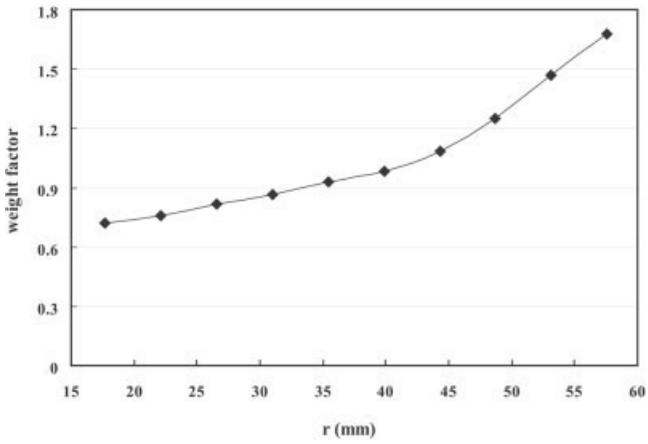

Figure 9 Weight factor of residual stress versus radial distance.

where WF_i and ΔCS_i are weight factor and critical speed increase at each position, respectively.

Selecting the weighted stresses, which are obtained by multiplying initial stresses by the weight factor, as objective values, residual stress values were optimized to bring them close to the weighted stresses. Melt temperature, filling speed, and packing pressure were the design parameters considered; mold temperature was not considered, since it has little effect. Response surface methodology[32] and conjugate gradient method[33] were used for the optimization. Further details of the optimization can be found in the Appendix.

The initial and optimized process conditions are shown in Table V, and the residual stresses under each process condition are shown in Figure 10. As can be seen, the residual stresses under the new optimized process condition decrease at inner radii and increase at outer radii. Figures 11 and 12 show the change of birefringence and critical speed: the critical speed increased by about 10 Hz for the rotating speeds considered, and the birefringence decreased, especially at the inner radius region by more than 30%.

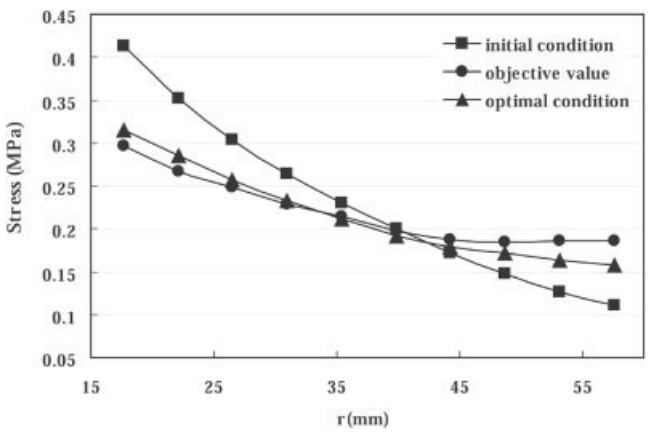

Figure 10 Objective value and residual stresses under initial and optimal process conditions.

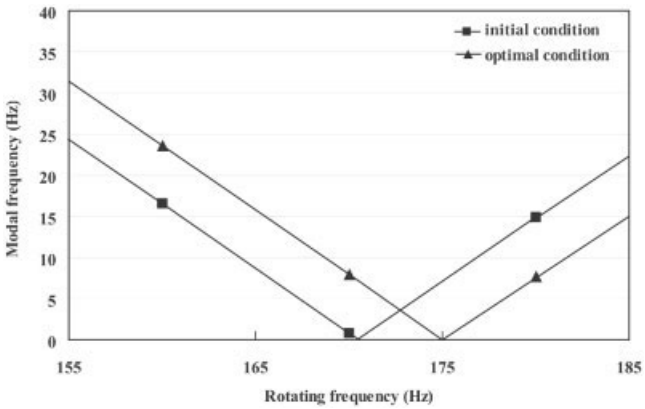

Figure 11 Critical speed for initial and optimal process condition versus rotating frequency.

CONCLUSIONS

Injection molding is a very complex process, and the behavior of the resin within the mold is difficult to characterize. Using computer simulation of the injection molding process, modal analysis of disk, and experimental design of processing condition, we have proposed a way to improve the optical quality and stability of disks.

The conclusions are as follows:

1. The melt temperature and the associated solidified thickness are the controlling factors on development of the birefringence and the stresses within the molded part. When the melt temperature increases, the birefringence and the residual stress decrease. On the other hand, the birefringence and residual stresses are little affected by the mold temperature.
2. For a higher filling speed, gapwise velocity, the associated shear rate, the shear stress, and birefringence increase at core region. However, the contact time with the mold decreases when the filling speed increases. So, the thickness of solid-

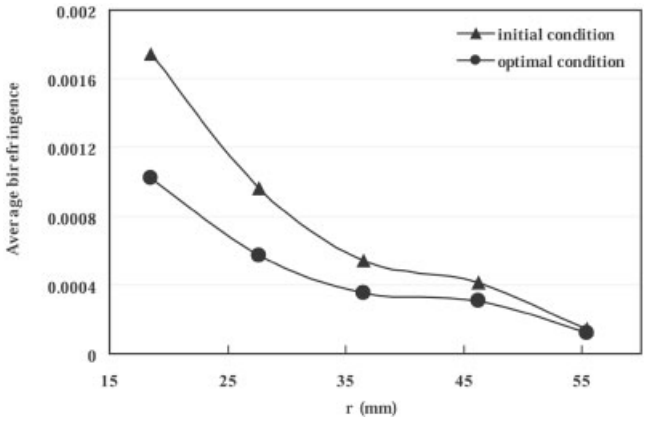

Figure 12 Radial profiles of the average birefringence for the initial and optimized process conditions, respectively.

TABLE VI
Design Parameters Data of 2nd Order Response Surface Design for the Residual Stress

Linearized factor level	−2	−1	0	1	2
X1 (°C)	230	235	240	245	250
X2 (s)	0.5	0.875	1.25	1.625	2
X3 (%)	40	52.5	65	77.5	90

X1, melt temperature; X2, filling time; X3, packing pressure.

ified layer decreases and then more stress relaxation occurs. Therefore, the effect of filling speed, presenting a combination of these two reactions, on residual stresses and birefringence varies as a function of the distance from the gate.

3. With increased packing pressure, the birefringence and the stress increase significantly near the gate area. However, the effect of packing pressure is small at the outer radius area, since there is little and slow material flow at this area in the packing stage.
4. Residual stresses at the outer position away from the gate increase the critical speed. By using the rise in the critical speed, weight factor is calculated. The weighted stresses serve as the objective values for optimization of residual stresses in terms of the process conditions. Under the new process condition proposed, both optical quality and stability were improved.
5. In future studies, this method for improving optical quality and stability may be applied to injection–compression molding process considering thermally-induced residual stresses and birefringence. From the viewpoint of the completeness and practicality of the study, experimental verification may be needed; this will also be included in the future study.

APPENDIX

With response surface methodology, residual stresses can be expressed as functions of design parameters. Using a central composite design, the second-order model of the residual stress is as follows:

$$Y(x_1,x_2,x_3) = \gamma_0 + \sum_{i=1}^{3}\gamma_i Z_i + \sum_{i=1}^{3}\gamma_{ij} z_i^2 + \sum_{i<1}^{3}\gamma_{ij} z_i z_j + e \tag{A1}$$

where γ_i, z_i, e are the regression coefficient, linearized factor level, and error term, respectively. Data of each factor used in the central composite design are shown in Table VI.

After the difference between objective values (weighted stresses) and Y is computed along the radial position, the objective function for optimization can be expressed as follows:

$$F(x_1,x_2,x_3) = \sum_{i=1}^{N}|Z_i - Y_i| \tag{A2}$$

where Z_i is weighted stress, which was obtained in the previous section.

To minimize this function, process conditions are optimized by the conjugate gradient method.

References

1. Leonov, A. I. Rheol Acta 1976, 15, 85.
2. Leonov, A. I.; Lipkina, E. H.; Paskhin, E. D.; Prokunin, A. N. Rheol Acta 1976, 15, 411.
3. Isayev, A. I.; Hieber, C. A. Rheol Acta 1980, 19, 168.
4. Baaijens, F. P. T. Rheol Acta 1991, 30, 284.
5. Flaman, A. A. Polym Eng Sci 1993, 33, 193.
6. Shyu, G. D.; Isayev, A. I. SPE ANTEC Tech Papers 1995, 41, 2911.
7. Chen, S. C.; Chen, Y. C. J Appl Polym Sci 1995, 55, 1757.
8. Chen, Y. C.; Chen, C. H.; Chen, S. C. Polym Int 1995, 40, 251.
9. Lee, Y. B.; Kwon, T. H.; Yoon, K. H. Polym Eng Sci 2002, 42, 2246.
10. Lee, Y. B.; Kwon, T. H.; Yoon, K. H. Polym Eng Sci 2002, 42, 2273.
11. Yoon, K. H. Korean J Rheol 1995, 7, 19.
12. Kang, S. I.; Kim, J. S.; Kim, H. Opt Eng 2000, 39, 689.
13. Lamb, H.; Southwell, R. V. Proc Royal Soc 1921, 99, 272.
14. Mote, C. D. ASME J Eng Ind 1965, 89, 258.
15. Mote, C. D.; Szymani, R. Shock Vib Digest 1978, 10, 15.
16. Dugdale, D. S. Int J Prod Res 1966, 4, 237.
17. Parker, R. G.; Mote, C. D. J Sound Vib 1991, 145, 95.
18. Renshaw, A. A. J Sound Vib 1998, 210, 431.
19. Iwan, W. D.; Moeller, T. L. ASME J Appl Mech 1976, 43, 485.
20. Adams, G. G. Int J Mech Sci 1987, 29, 525.
21. Renshaw, A. A. Trans ASME 1998, 65, 116.
22. Park, S. J.; Kim, S. K.; Lee, C. Y. SPIE (Optomech Eng Vib Control) 1999, 3786, 106.
23. Janeschitz-Kriegl, H. Polymer Melt Rheology and Flow Birefringence; Springer: Berlin, 1983.
24. Taguchi, G. System of Experimental Design; UNIPUB: White Plains, New York, 1987.
25. Peter, K. Flow Analysis of Injection Molds; Hanser: New York, 1995; Chapters 5–6.
26. Chiang, H. H.; Hiber, A.; Wang, K. K. Polym Eng Sci 1991, 31, 116.
27. Chiang, H. H.; Himasakhar, K.; Santhanam, N.; Wang, K. K. J Eng Mater Tech 1993, 115, 37.
28. Shyu, G. D.; Isayev, A. I.; Lee, H. S. Korea-Aust Rheo J 2003, 15, 159.
29. Irons, J. J Sound Vib 1988, 121, 481.
30. Chung, J. T.; Kang, N. C., Lee, J. M. KSME J 1996, 10, 138.
31. Arfken, G. Mathematical Methods for Physicists; Academic Press: San Diego, 1985.
32. Angela, D.; Daniel, V. Design and Analysis of Experiments; Springer-Verlag: New York, 1999.
33. Ashok, D. Tirupathi, R. Optimization Concepts and Applications in Engineering; Prentice Hall: Upper Saddle River, New Jersey, 1999.